Thermodynamics and Kinetics of Na-Ion Insertion into Hollandite-TiO_2 and O3-Layered $NaTiO_2$
An Unexpected Link between Two Promising Anode Materials for Na-Ion Batteries

Vasileiadis, Alexandros; Wagemaker, Marnix

DOI
10.1021/acs.chemmater.6b03928

Publication date
2017

Document Version
Final published version

Published in
Chemistry of Materials

CHEMISTRY OF MATERIALS

Article

pubs.acs.org/cm

Thermodynamics and Kinetics of Na-Ion Insertion into Hollandite-TiO_2 and O3-Layered $NaTiO_2$: An Unexpected Link between Two Promising Anode Materials for Na-Ion Batteries

Alexandros Vasileiadis and Marnix Wagemaker*

Department of Radiation Science and Technology, Delft University of Technology, Mekelweg 15, 2629JB Delft, The Netherlands

ABSTRACT: First principle DFT calculations are used to study the thermodynamic and kinetic properties of Na-ion insertion in TiO_2 hollandite, a potential anode for Na-ion batteries. The experimentally observed phase transformation from tetragonal TiO_2 ($I4/m$) to monoclinic $Na_{0.25}TiO_2$ ($I2/m$) is confirmed. At high Na-ion concentrations the calculated formation energies predict a first-order phase transition toward the layered O′3-$Na_{0.68}TiO_2$ structure. Further sodiation initiates a solid solution reaction toward the layered O3-$NaTiO_2$ phase, which was recently brought forward as a promising anode for Na-ion batteries. This transformation irreversibly transforms the one-dimensional hollandite tunnel structure into the layered structure and potentially brings forward an alternative route toward the preparation of the hard to prepare O3-$NaTiO_2$ material. Energy barrier calculations reveal fast Na-ion diffusion at low concentrations and sluggish diffusion upon reaching the $N_{0.25}TiO_2$ phase, rationalizing why experimentally the $Na_{0.5}TiO_2$ phase is not achieved. Detailed analysis of the kinetic behavior in the hollandite structure via molecular dynamics simulations reveals the importance of correlated atomic motions and dynamic lattice deformations for the Na-ion diffusion. In addition, exceptional Na-ion kinetics were predicted for the layered O′3-$Na_{0.75}TiO_2$ phase through a dominating divacancy hopping mechanism.

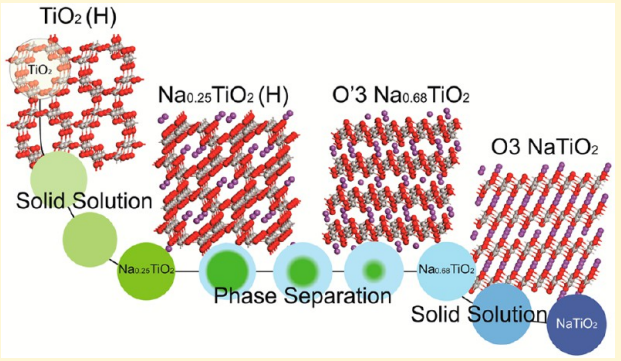

1. INTRODUCTION

The high gravimetric and volumetric energy density of Li-ion batteries revolutionized modern society by enabling mobile applications such as laptops, tablets, and mobile phones. However, the increasing demand for Li-ion batteries by the development of electrical cars and static storage, for instance in houses, challenges the practical abundance of lithium world-wide.[1,2]

A highly promising alternative charge carrier, already considered by the scientific community decades ago, is sodium being much more abundant and displaying comparable redox potentials and insertion behavior[3,4] compared to lithium. Sodium, however, has a larger ionic radius compared to lithium imposing larger volume changes on the host structure lattice which is detrimental for the cycle life.[5] Although several materials have been reported as candidates for Na-ion positive electrodes, Na-ion anode materials are scarcely reported on. Because Na-ion intercalation into graphite layers appears not possible,[6] research focuses mainly on other carbonaceous materials such as hard carbons[7,8] and petroleum cokes,[9] while noncarbonaceous alloys[10] and vanadium oxides[11,12] are investigated as well. TiO_2 polymorphs are well studied as negative electrode materials for Li-ion batteries, primarily because of the success of spinel $Li_4Ti_5O_{12}$[13−16] and anatase[17−20] and secondarily because of rutile,[21] layered TiO_2,[22] brookite, and ramsdellite.[23] Recently those polymorphs were also investigated as potential negative electrode materials for Na-ion insertion.[24−28]

Among them, the layered O3-$NaTiO_2$ was identified as one of the most promising Na-ion anode candidates due to its exceptional electrochemical performance and the ability to intercalate Na-ions without large volume changes (<1%).[25] Early studies of the layered O3-$NaTiO_2$ resulted in limited intercalation behavior[29] and a substantial diffusion barrier.[30] Recently Wu et al.[25] showed that reducing the water content and expanding the voltage window results in excellent capacity (150 mAh/g) and reversibility between the $Na_{0.5}TiO_2$ and $NaTiO_2$ phases. The same group[25] performed DFT calculations to determine the energy barriers indicating exceptionally good kinetic behavior. In situ X-ray diffraction revealed an O3 to O′3 phase transition[25] where the O′3 notation refers to the structures resulting from the monoclinic distortion of the O3 layered $NaTiO_2$.[31] This is a very common reduction among O3 type compounds, and it is accounted to Na vacancy ordering.[31] The O3 notation refers to the type of oxygen coordination of the inserted ion (O for octahedral) and the repetition number of transition metal stacks (3) in the layered structure.[25]

A much less investigated polymorph is TiO_2 hollandite, noted as TiO_2 (H), that was first reported in 1989[32] where

Received: September 15, 2016
Revised: November 10, 2016
Published: December 6, 2016

DOI: 10.1021/acs.chemmater.6b03928
Chem. Mater. 2017, 29, 1076−1088

potassium was extracted from the original K_xTiO_2 ($0.13 < x < 0.25$) structure. The tetragonal hollandite structure is indexed by the $I4/m$ space group symmetry (Figure 1) for which the

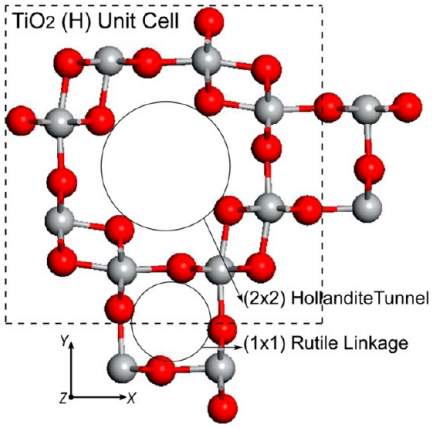

Figure 1. Crystal structure of TiO_2 (H), Ti atoms are located in the center of the TiO_6 octahedra that share both edges forming the large 2 × 2 tunnel, rutile linkage channels connect the hollandite channels, the dashed line encloses one unit cell, red spheres represent O atoms, while gray ones represent Ti atoms.

large hollandite 2 × 2 channel aligned with the *c*-axis was immediately recognized as a potential pathway for ion diffusion and insertion. The large 2 × 2 channels are linked via rutile channels that are referred to as rutile linkage. The Li-ion insertion properties were investigated by Noailles et al.[33] reporting a voltage profile around 1.5 V, low reversibility, high polarization, and capacities far below the theoretical capacity of 335 mAh/g offered by the $Ti^{3+/4+}$ redox couple. The initial capacity of 160 mAh/g was never recovered, and a reversible capacity of only 36 mAh/g resulted. Gutierrez-Florez et al.[34] managed to obtain a higher reversible capacity. Much later Sakao et al.[35,36] re-examined hollandite TiO_2 (H) managing a reversible capacity of 147 mAh/g for 50 cycles. Sakao et al.[36] demonstrated that a larger K content (residual from the synthesis) plunges the electrochemical performance explaining the early results of Noailles et al.[33] About four Li-ions per unit cell ($Li_{0.5}TiO_2$) reside in the hollandite 2 × 2 channel, while the 1 × 1 rutile linkage remains empty. Upon lithiation the symmetry reduces to monoclinic ($I2/m$) due to the structural distortion induced by Li-ion ordering in the 2 × 2 channel, the consequence of cation repulsions.[33]

Na-ion insertion in TiO_2 (H) has been investigated by Perez-Florez et al.[37] reporting a reversible capacity of 85 mAh/g after an initial first discharge of 280 mAh/g. The proposed reversible Na-ion insertion mechanism starts with a solid solution reaction followed by a phase transition from the original hollandite tetragonal symmetry ($I4/m$) to the monoclinic ($I2/m$) reaching the composition $Na_{0.25}TiO_2$ with a relatively small volume change upon Na-ion insertion of 1.1%. Up to date it is unclear why the practical capacity appears to be limited to the $Na_{0.25}TiO_2$ composition and what happens beyond this composition and how that effects the structure and Na-ion kinetics. To establish the theoretical possibilities and limitations as a Na-ion insertion electrode material computational approaches may be of large interest. In the present work, DFT is used to predict and reveal the structure, thermodynamics, and Na-ion kinetics of TiO_2 (H) upon Na-ion insertion which to the best of our knowledge has not been attempted previously. The resulting formation enthalpies and derived voltages vs Na/Na^+ give insight into the insertion mechanism and structural evolution of the material. Energy barrier calculations shed light on what limits the performance of the TiO_2 (H) as an anode material for Na-ion batteries. Thorough investigation of the kinetic mechanisms reveals the importance of correlated atomic motions and lattice dynamics for ionic diffusion which is suggested to be of general importance for computational research. At high Na-ion concentrations the DFT results predict a first-order phase transition toward the O3 layered $NaTiO_2$. Although this thermodynamic path cannot be induced during battery cycling, it may provide a novel and more facile route toward the synthesis of the layered $NaTiO_2$ material which has recently been shown to have excellent Na-ion electrode properties. Thereby, the present ab initio study provides insight in two potential Na-ion electrode materials TiO_2 (H) and layered O3 Na_xTiO_2.

2. COMPUTATIONAL METHODS

DFT calculations were performed in the plane wave code VASP.[38] Valence-core interactions were probed with the projector augmented wave approach (PAW)[39] with cores of [Ar] for Ti, [He] for O, and [Ne] for Na. All calculations were integrated with the gradient-corrected (GGA) exchange correlation functional of Perdew et al.[40] and treated with the tetrahedron method with Bloch corrections. The titanium oxide host structures were optimized by relaxation of their respective experimental values obtained from the literature. Structure relaxations required a high energy cutoff of 520 eV and a Monkhorst–Pack k-point set to achieve convergence better than 2 meV/atom. Total energies resulted from a second self-consistent calculation such that the k-point grid can recover from the lattice changes upon Na insertion. For comparison selected calculations were performed using a Hubbard correction parameter (DFT+U method[41−43]) U_{eff} = 4.2 eV to account for the tendency of regular DFT calculations to overestimate the electron delocalization of d and f orbitals, which is well-known for systems with strongly localized and correlated electronic ground states.[41,44−46] In addition, a few Li-ion configurations were studied to probe differences between the Li-ion and Na-ion charge carriers. To predict the activation energy for Na-ion hopping in the TiO_2 (H) the nudge elastic band method[47] was applied using the climbing image modification.[48,49] In this way a string of Na-ion positions that describe the possible diffusion pathway is relaxed to the minimum energy path. The total energy difference between the saddle point and the initial local minima represents the activation barrier (E_a) of the Na-ion hopping. In order to capture phase transformations and/or the importance of atomic motions upon migration, we also implemented the solid state nudge elastic band method (ss-NEB)[50] that allows the lattice parameters to relax. All nudge elastic band (NEB) barrier calculations were executed in large supercells (1 × 1 × 3) with lattice parameters exceeding 10 Å in order to avoid interactions between images of Na being moved.[51] Additionally, to obtain a concrete and complete picture of the kinetics we performed molecular dynamic (MD) calculations for 190 up to 400 ps with a 2 fs time step at 600 K. By determining the amount of hops the mean jump rate ν according to $\nu = J/(Nt)$ was calculated where J represents the number of transitions in the MD simulation, N is the total number of Na-ions in the supercell, and t is the total simulation time. The respective activation barriers for the various jumps are calculated using transitional state theory formulated as $E_a = -kT \ln(\nu/\nu_0)$[52] where ν_0 represents the attempt frequency, typically assumed to be 10^{13} s^{-1},[53] k is Boltzmann constant, and T is the temperature. Diffusion coefficient calculations were performed based on the random-walk atomistic model.[51,52,54,55] The diffusion coefficient can be expressed as

$$D = \gamma\lambda^2\Gamma$$

DOI: 10.1021/acs.chemmater.6b03928
Chem. Mater. 2017, 29, 1076−1088

where $\gamma = 1/N$ with N matching the number of directions in the crystal toward the ion can hop to, λ represents the distance between the jumps, and Γ is the jump frequency where the temperature dependence is introduced as

$$\Gamma = ue^{-\frac{\Delta G}{kT}} = ue^{-\frac{\Delta S}{k}}e^{-\frac{\Delta H}{kT}}$$

where u is the vibrational or attempt frequency (s^{-1}). The vibrational frequency is typically assumed to be 10^{13} s^{-1}.[53] Finally, we can write

$$D_{Na} = D_0 e^{-\frac{E_a}{RT}}$$

with

$$D_0 = \gamma\lambda^2 ue^{-\frac{\Delta S}{k}}$$

a temperature independent pre-exponential. The last term is a very small positive number and can be ignored. Finally, when applicable, an estimate of the self-diffusion coefficient was obtained based on the mean square displacement (MSD) resulting from the molecular dynamic calculations according to the formula $D = \mathrm{MSD}/(2Nt)$[56] where t represents the total simulation time, and N is the dimensionality of the system.

3. RESULTS AND DISCUSSION

3.1. Dilute-Limit Na-Ion and Li-Ion Insertion in TiO_2 (H). The TiO_2 (H) structure was optimized starting at the experimental values[32] using a 6 × 6 × 8 k-point grid. Total energy calculations upon Na and Li ion insertion were performed in a 1 × 1 × 2 supercell that contains in total 48 host atoms ($Ti_{16}O_{32}$). The resulting lattice parameters, see Table 1, were slightly larger than those experimentally observed, an overestimation that is typically encountered when using the GGA method.[57]

Table 1. Experimental vs DFT Predicted Lattice Parameters of the Hollandite TiO_2 Unit Cell

TiO_2 (H)	a (Å)	b (Å)	c (Å)	α, β, γ (deg)
GGA	10.302	10.302	2.980	90
experimental	10.161(3)	10.161(3)	2.910(1)	90

The structure reveals the presence of 1 × 1 rutile channels and the larger 2 × 2 hollandite channels, together providing six interstitial positions to accommodate cations as illustrated by Figure 1. The first three interstitial sites, Wyckoff notations 4c, 2a, 8h′, are coplanar in the xy-plane intersecting the z-axis at z = 0.5, as shown in Figure 2a. The next two interstitial sites, Wyckoff notations 8h and 2b, are coplanar in the xy-plane intersecting the z-axis at z = 0, and finally the 4e site is positioned at (0,0,z) as shown in Figure 2b. According to Tompsett[58] the 8h′ and 8h sites can be distinguished despite the fact that they hold the same Wyckoff position because the 8h′ site is positioned very close to the coplanar 2a position creating a different coordination compared to that of the 8h site.[58] Na-ion and Li-ion insertion was simulated by accommodating the cations in all available lattice sites and allowing relaxation of the ionic positions and lattice parameters, as well as allowing symmetry changes toward the lowest energy configuration.

Introducing a single Na-ion in the $Ti_{16}O_{32}$ supercell results in the $Na_{0.06}TiO_2$ composition, representing the dilute limit of Na-ion insertion, the relaxation results of which are presented in Table 2. At dilute compositions Na-ions prefer the center of hollandite tunnel (2a site), where in all cases sodium inserted in the coplanar 8h′ position relaxed toward the 2a site. For the 4e

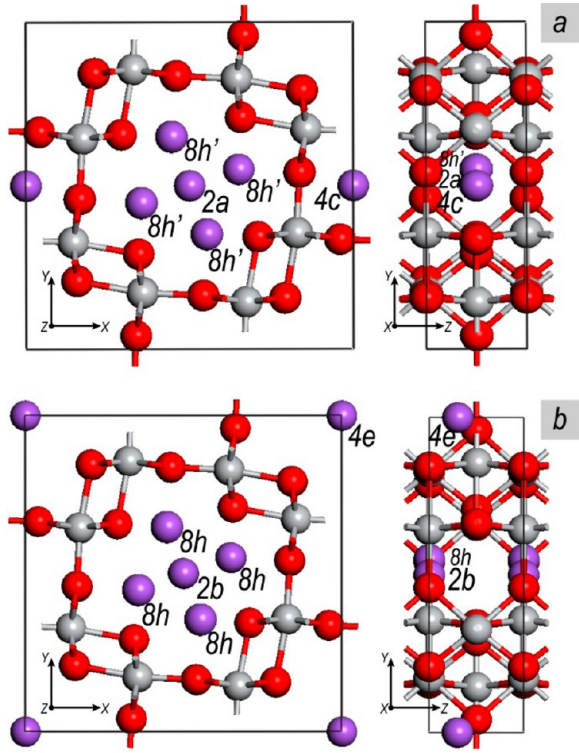

Figure 2. a: 2a, 4c, and 8h′ coplanar positions, red spheres represent O atoms, gray spheres represent Ti, and purple spheres represent Na-ions. b: 2b, 8h, and 4e positions, red spheres represent O, gray spheres represent Ti, and purple spheres represent Na-ions.

Table 2. Relative Formation Energies of Na-Ion and Li-Ion Occupancy of the Different Interstitial Sites in the $(Na,Li)_{0.063}Ti_{16}O_{32}$ Hollandite Supercell[b]

ion site	ΔE (Na-ion) (meV) DFT	ΔE (Na-ion) (meV) DFT+U (4.2)	ΔE (Li-ion) (meV) DFT
2a	0	0	310
8h′	1[a]	4[a]	4
4e	38[a]	15[a]	310[a]
8h	84	84	0
2b	143	169	618
4c	3348	3431	1040

[a]In those cases the Na/Li-ion relaxed toward the nearby 2a position, resulting either in exactly the 2a position (and formation energy) or a position very near to the 2a position (with a slightly larger formation energy). [b]Energies are given with respect to the lowest energy site. In addition for the Na-ion case both DFT and DFT + U (4.2) calculations were performed.

(0,0,z) position the relaxation depends on the z-coordinate of the Na-ions. For (0,0,z < 0.3) the Na-ions relaxes toward the lowest energy 2a site, and for z > 0.3 the Na-ions remain near the starting (4e) position, a configuration with a slightly higher energy, indicating the presence of a barrier for the relaxation toward the 2a site. In contrast, for Li-ion insertion at the dilute limit ($Li_{0.06}TiO_2$) the lowest energy Li-ion position is the 8h site followed by the h′ site, both closer to the channel wall leading to short Li−O distances (Figure 3a).

The different positions in the channel can be accounted to the difference in Na-ion and Li-ion radius. In these structures where the bonds are largely ionic, the coordination number of a cation within a polyhedron of anions depends on the relative size of the cation and the anion. As a general rule, the most

DOI: 10.1021/acs.chemmater.6b03928
Chem. Mater. 2017, 29, 1076−1088

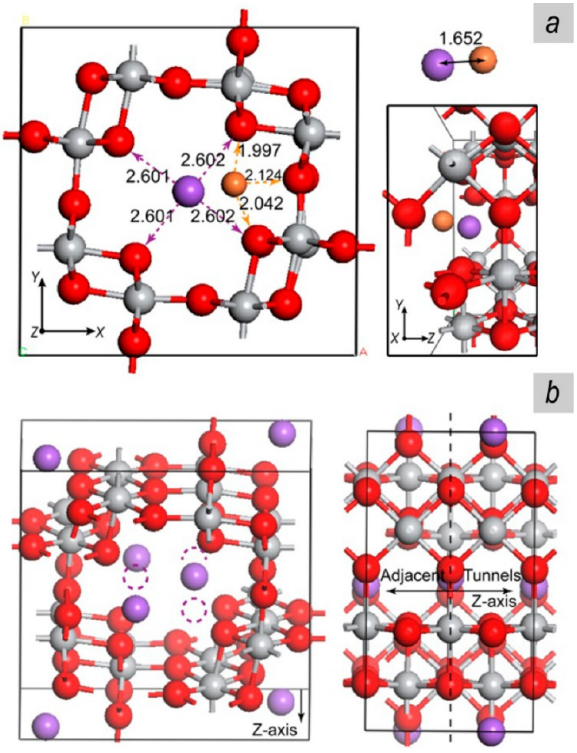

Figure 3. a: Na-ion versus Li-ion positions in the dilute limit $(Na,Li)_1Ti_{16}O_{32}$. The atomic distances are reported in Angstroms, purple spheres represent Na-ions, orange spheres represent Li-ions, red spheres represent O atoms, and gray spheres represent Ti atoms. b: Lowest energy configuration at intermediate Na concentration $Na_{0.25}TiO_2$ where Na-ions occupy alternating 8h positions forming a zigzag chain of Na-ions in the 2 × 2 hollandite channels, maximizing the Na−Na distances driven by Coulombic repulsion, purple spheres represent Na-ions, red spheres represent O atoms, and gray spheres represent Ti atoms.

preferable coordination occurs when the cation size exactly fits or is slightly larger than the interstice geometrical space offered by the polyhedron. Cations with smaller ionic radius will be able to "rattle" in the relatively large interstitial space making the structure energetically unfavorable and are most stable at the next lower coordination.[59] Even though Pauling's first rule[59] is an oversimplification, treating atoms as hard spheres in a closed packed arrangement, it appears to apply consistently in all Ti oxide structures.[60−65] The Li-ion radius allows a maximum 6-fold coordination (octahedral position) or a 4-fold coordination (tetrahedral) with a small energy penalty. Depending on the local environment, however, the tetrahedral coordination could be more stable compared to the octahedral coordination as illustrated by the rutile[61] and LTO[66,67] structures. When residing in the 2a position of the 2 × 2 hollandite channel the Li-ion is coordinated by 4 primary and 4 secondary (8 oxygen atoms in total) which introduces a large energy penalty forcing the Li-ion toward the tunnel wall. The resulting Li−O interatomic distances for the 3 closest oxygen atoms are between 1.997 and 2.124 Å, similar to what is found in other oxide hosts like TiO_2 anatase (1.940 to 2.245 Å)[60] $LiCoO_2$ (2.11 Å)[68] or LFP (2.095 to 2.167 Å).[69] In contrast, Na-ions are large enough to be accommodated in the 2a position (previously occupied by an equally large potasium ion during the synthesis process to stabilize the 2 × 2 tunnel).

The large formation energy for the Na-ion and Li-ion located at the 4c position, within the rutile linkage channel, indicates that this position is unlikely to occur at low concentrations. The octahedral position offered by the rutile channel is too small compared to the Na-ion radius leading to significant lattice distortions (1.9% volume change) which raises the energy compared to the Li-ion. Na-ion insertion in the octahedral rutile position was further investigated by performing DFT calculations of Na-ion insertion in the rutile TiO_2 structure. The rutile TiO_2 structure is strongly distorted by the Na-ion occupancy of the octahedral position causing volume changes of 2.2% even at the small Na-ion concentration in the $Na_{0.06}TiO_2$ composition. The resulting Na−O distances after relaxation amount to 2.04 and 2.21 Å, values practically equivalent with that of the distorted 4c site in the hollandite structure when occupied by a Na-ion (2.05 and 2.23 Å). The DFT calculations predict a negative insertion voltage (−0.5 V vs Na^+/Na - $Na_{0.06}TiO_2$) for Na-ion insertion in rutile TiO_2 indicating Na-ion insertion is energetically unfavorable.

Further Na-ion insertion affects the formation energies of the ionic positions drastically. Compositions above $Na_{0.125}TiO_2$ cause Na-ion occupation in adjacent 2 × 2 hollandite channels, forcing Na-ions previously occupying the 2a site to shift toward the 8h position. In the $Ti_{16}O_{32}$ hollandite supercell, which contains four 2 × 2 channels, this effect occurs when a third Na-ion is inserted ($Na_{0.19}TiO_2$). Adding one additional Na-ion in the hollandite superstructure results in $Na_{0.25}TiO_2$, which is the lowest energy configuration and is characterized by a zigzag-8h occupation along the *c*-axis (shown in Figure 3b), thereby having half of the 8h positions occupied.

Coulombic forces appear responsible for this configuration as the 2a-2a distance between adjacent tunnels is around 3 Å, whereas for the diagonally Na-ion occupied 8h positions in $Na_{0.25}TiO_2$ are separated by 3.75 Å. Electrostatic repulsion might not be the only criterion as the 8h′-8h′ zigzag configuration can provide an even greater distance between the Na ions (4.3 Å). Apparently, the oxygen coordination provided by the 8h position is more favorable compared to the 8h′ position.

3.2. The Monoclinic $Na_{0.25}TiO_2$ (H) Phase. The DFT predicted $Na_{0.25}TiO_2$ phase is in good agreement with the experimental result first reported by Perez-Florez et al.[37] The starting TiO_2 (H) tetragonal *I*4/*m* symmetry is reduced to the monoclinic *I*2/*m* symmetry resulting in a significant reduction of the b-lattice parameter, 3% as determined by the present DFT calculations compared to 2.6% reported experimentally,[37] along with an increase in the β^o angle. For X-ray diffraction this results in splitting of the hollandite TiO_2 {020} reflection into the {200} and {002} reflections of the $Na_{0.25}TiO_2$ monoclinic lattice. In Table 3 the experimentally determined lattice parameters are compared to the values predicted by the present DFT calculations. Based on the DFT predicted structures the powder diffraction patterns were calculated, shown in Figure 4b, illustrating good agreement with the experimentally obtained patterns.[37] Figure 4b demonstrates the phase transition between the tetragonal and monoclinic structures by the splitting of the second and third reflections.

Interatomic distances between Ti and O atoms are between 1.963 and 2.046 Å, while distances between Na-ions and the closest O atoms are between 2.392 and 2.471 Å for both the relaxed experimental and predicted phase. The diagonal distance connecting the two Na-ions is 3.748 Å in the DFT predicted phase and 3.762 in the experimental (DFT-relaxed)

DOI: 10.1021/acs.chemmater.6b03928
Chem. Mater. 2017, 29, 1076−1088

Table 3. Comparison of the Monoclinic $Na_{0.25}TiO_2$ Unit Cell Parameters between the Experimental and Presently Predicted Values[a]

method	experiment values[37]	predicted values upon sodiating with DFT
s.g.	*I*2/*m*	*I*2/*m*
a (Å)	10.4509(14)	10.585
b (Å)	2.9674(3)	2.9705
c (Å)	9.88497(11)	9.988
β (Å)	90.683(2)	90.55
Δ*V*	1.1%	0.72%

[a]The volume change is calculated with respect to the empty host. Note that the b-lattice parameter of the tetragonal phase changes into the c-lattice parameter in the monoclinic symmetry.

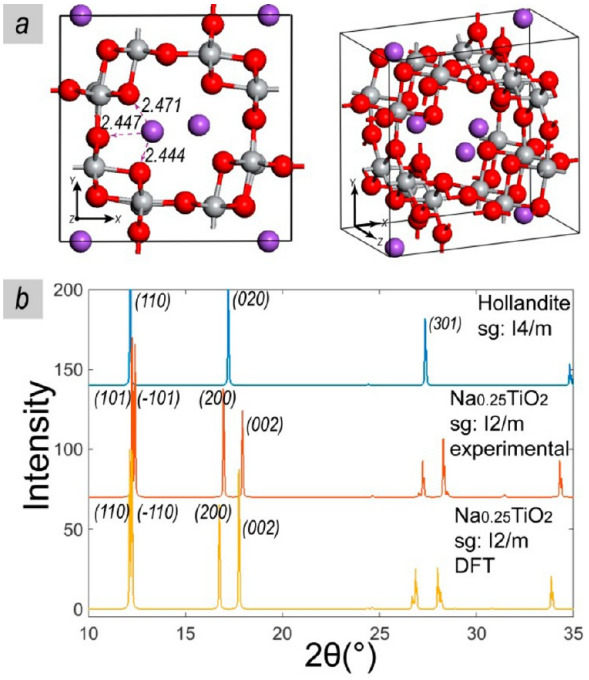

Figure 4. a: $Na_{0.25}TiO_2$ as predicted by DFT, corresponding to a specific capacity of 85 mAh/g of specific capacity, where red balls represent O atoms, gray balls represent Ti, and purple balls represent Na ions. The arrows indicate the distance in Angstroms between Na ions and nearest oxygen atoms at the wall of the tunnel. b: From top to bottom, the calculated XRD pattern of the empty hollandite structure predicted by DFT, the calculated pattern based on the experimental XRD lattice parameters of $Na_{0.25}TiO_2$,[37] and the calculated XRD pattern of the DFT predicted $Na_{0.25}TiO_2$ phase.

phase. The presence of nearby Na-ions in adjacent 2 × 2 channels reduces the Na−O distance when compared to the dilute limit ($Na_{0.6}TiO_2$), effectively pushing Na-ions toward the wall of the channel. The 2a toward 8h position shift appears responsible for the tetragonal to monoclinic phase transition as the b-lattice parameter reduction, and the β^o angle increase at the $Na_{0.19}TiO_2$ composition is observed. This result is consistent with XRD data[37] reporting broadening of the peaks for increasing Na content above $x = 0.17$. In Figure 4a the lowest energy $Na_{0.25}TiO_2$ monoclinic phase is presented.

3.3. Formation Enthalpies and the Voltage Profile. To study the thermodynamic stability of the Na_xTiO_2 intercalation system the formation enthalpies of 72 symmetrically inequivalent configurations are plotted in Figure 5a according to[70−72]

$$E_{form} = E - xE_{NaTiO_2} - (1 - x)E_{TiO_2}$$

The formation enthalpy, E_{form}, reflects the relative stability of each configuration with respect to phase separation into a fraction x of $NaTiO_2$ and a fraction $(1-x)$ of TiO_2. E is the energy of a specific arrangement at a concentration x, E_{NATiO_2} is the energy of the titanium structure while accommodating the maximum amount of Na ions (in this case the maximum reference phase responds to a 1:1 Na/Ti ratio), and E_{TiO_2} is the total energy of the empty titanium dioxide host. Thereby, negative formation energies, energies below 0 eV, are thermodynamically favorable compared to the reference phases and thus are not likely to occur. The convex hull is constructed by the line connecting the most stable structures at each composition giving insight in the relative stability of intermediate phases and the structural evolution upon Na-ion insertion.

All intermediate compositions up to $Na_{0.25}TiO_2$ (Figure 5a) are at or very near the convex hull predicting at room temperature a solid solution transformation from the tetragonal to monoclinic phase. The reduction in symmetry is a consequence of the gradual change in the interaxial lattice angle β initially at 90° for the tetragonal starting phase. On the atomic scale this is initiated by the shift in Na-ion occupancy from the 2a to 8h position upon sodiation. Several electrode materials lithiate/sodiate either partially or completely via a solid solution mechanism leading to a gradual change in the unit cell edge length. To the best of our knowledge, Na-ion insertion in TiO_2 hollandite is the first where a solid solution reaction results in a change in symmetry through the gradual change in interaxial lattice angle, although this is conceptually not different from a gradual change in the unit cell edge length. This result is in agreement with experimental observations by XRD[37] where the gradual shift in the diffraction peaks between $Na_{0.17}TiO_2$ and $Na_{0.25}TiO_2$ indicates a solid solution reaction resulting in a biphasic region of unreacted and reacting phases. Note that the absence of a voltage plateau in the voltage profile also suggests a solid solution mechanism. The difference in formation energy between configurations with Na in the 2 × 2 channel and configurations with at least one Na in the 1 × 1 rutile channel appears constant (210 meV) with respect to the Na insertion into the 2 × 2 channels in the tetragonal range ($0 < x < 0.125$) and lower but still constant (165 meV) in the monoclinic regime ($0.125 < x < 0.25$).

Interestingly, further sodiation reveals a two phase reaction mechanism between the monoclinic $Na_{0.25}TiO_2$ and $Na_{0.68}TiO_2$ structures. During this phase transition the hollandite skeleton changes completely toward a layered structure that is recognized to be the O′3 layered $Na_{0.68}TiO_2$ phase, indexed by the *C*2/*m* symmetry.[73] Formation of the layered structure requires the Na-ions to enter the rutile linkage tunnels along the *z*-direction. Due to the large distortions caused by this the Ti−O bonds will break, opening the lattice to form Ti slabs as shown in Figure 6a, b. This transformation appears irreversible because removal of the Na-ions from the layered structure does not result in the original hollandite lattice. Further Na-ion insertion of the layered $Na_{0.68}TiO_2$ structure proceeds through a solid solution reaction up to the fully sodiated structure (O3-$NaTiO_2$) which was recently reported as a promising anode for Na-ion batteries.[25] Thereby TiO_2 (H) can be fully sodiated to the theoretical maximum capacity of 335 mAh/g offered by the Ti^{4+}/Ti^{3+} redox couple. Clearly, the irreversibility of this

DOI: 10.1021/acs.chemmater.6b03928
Chem. Mater. 2017, 29, 1076−1088

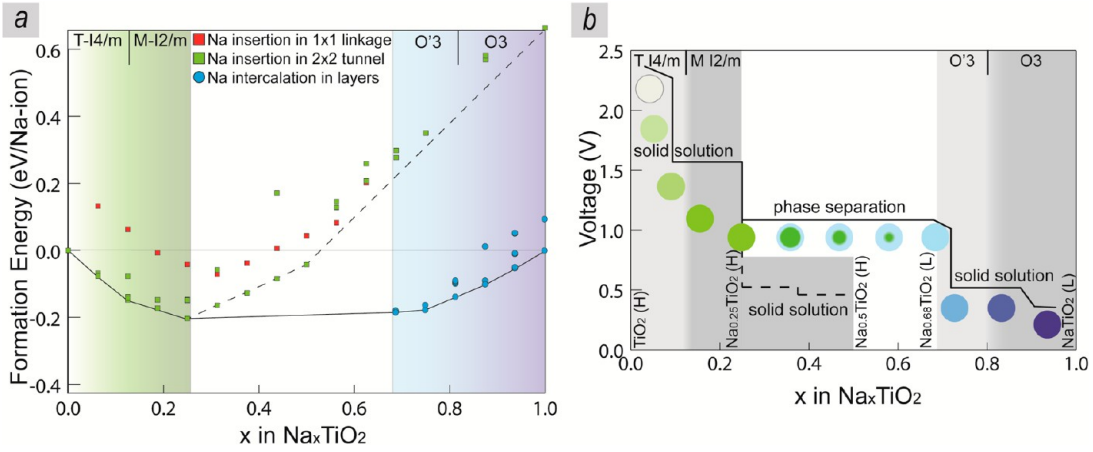

Figure 5. a: Formation energies and convex hull upon Na insertion in the TiO_2 (H) structure. Squares refer to configurations where the hollandite skeleton is preserved, and they are colored green for Na insertion in the 2 × 2 channels or red for at least one Na inserted in the 1 × 1 rutile linkage. Blue circles correspond to the layered structure, the solid line represents the convex hull, and the dashed line represents the convex hull without considering the monoclinic to layered phase transition. b: Voltage profile for Na-ion insertion into TiO_2 (H) resulting from the DFT energy calculations. At approximately 1 V the constant voltage indicates a first-order phase transition leading to the layered $Na_{0.68}TiO_2$ phase. The dashed line indicates the voltage when the hollandite structure is maintained, as it appears in practice. (H) indicates the hollandite structure (either tetragonal or monoclinic), and (L) indicates the layered structure; T-*I*4/*m* stands for tetragonal and M-*I*2/*m* for the monoclinic lattice.

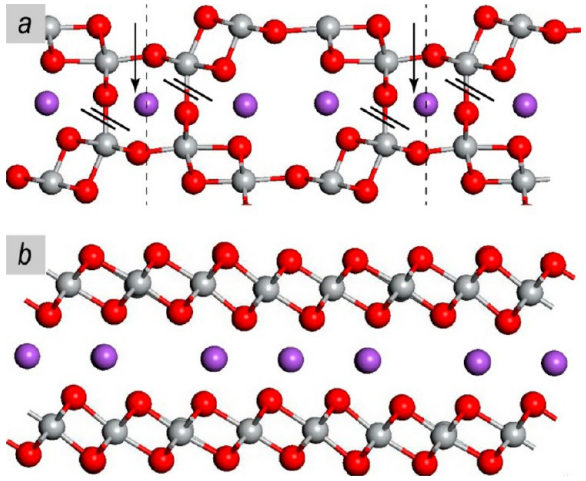

Figure 6. a: Na-ion configuration before relaxations ($Na_{0.68}TiO_2$) with Na-ions inserted in the rutile-linkage tunnel, as indicated by the black arrows. The black lines indicate the bonds that are broken by this configuration resulting in the layered structure. b: The layered $Na_{0.68}TiO_2$ structure. In both figures the red spheres represent O atoms, gray spheres represent Ti atoms, and purple spheres represent the Na-ions.

process prevents accessing this capacity reversibly, but Na-ion insertion of TiO_2 (H) may offer a novel route toward the layered $NaTiO_2$ material. The characteristics of the O3 layered $NaTiO_2$ predicted by DFT will be discussed in the next section.

The predicted phase transition toward the O3 layered Na_xTiO_2 structure appears not to occur during electrochemical Na-ion insertion[37] down to 0.2 V, although the formation energies in Figure 5a suggest it is energetically favorable to form at high Na-concentrations. This may be explained by the large energy required to insert Na-ions in the rutile linkage channels, as indicated by Figure 5a, which is necessary to break the Ti−O bonds, and additionally by a large kinetic energy barrier. The alternative is that the metastable hollandite structure is retained, as indicated by the dashed line in Figure 5. Perez-Florez et al.[37] reports a continuous evolution of the lattice parameters in the 0.75 to 0.5 V voltage range suggesting a solid solution reaction upon Na-ion insertion in the monoclinic phase, although no conclusive evidence for this was shown down to 0.2 V. It was assumed that Na-ion insertion above $x = 0.25$ is restricted due to the introduction of short Na−Na distances.[37] The present formation enthalpies predict that Na-ion insertion should be possible at least up to $x = 0.5$ in Na_xTiO_2 (Figure 5a) suggesting that the Na-ion kinetics, which will be addressed below, restricts the capacity of the hollandite TiO_2 structure. In the monoclinic solid solution regime the calculations predict a total volume change of 2.4% from the TiO_2 toward the $Na_{0.5}TiO_2$ composition. This is larger compared to the 1% volume change from the TiO_2 toward the $Na_{0.25}TiO_2$ composition but still relatively small suggesting that mechanical failure will not restrict the cycle life. The present calculations predict that Na-ion insertion proceeds through a solid solution reaction in the concentration range $0.25 < x < 0.5$ during which the monoclinic *b*-lattice parameter continuously decreases and the β^o angle increases in agreement with the observation by Perez-Florez et al.[37] The final monoclinic $Na_{0.5}TiO_2$ phase is characterized by the *I*2/*m* symmetry with lattice parameters a = 11.14 Å, b = 2.97 Å, c = 9.79 Å and an angle β = 90.6°. In this configuration, Na-ions reside in the 8h positions that are empty in the dilute zigzag configuration shown in Figure 3b. The presence of the extra Na-ions leads to shorter bonding to the oxygen atoms in the tunnel wall (2.281, 2.284, 2.349 Å) compared to the distances in the $Na_{0.25}TiO_2$ phase.

Based on the formation energies in Figure 5 the voltage profile at 0 K can be calculated. The potential difference between the positive and negative electrodes is determined by the difference in Na/Na^+ potential according to the Nerst equation:[71,74]

$$V(x) = -\frac{\mu_{Na}(x) - \mu_{Na}^{ref}(x)}{e}$$

The chemical potential is per definition the derivative of the free energy with respect to the ion concentration which, disregarding the entropy, leads to the following expression[74]

DOI: 10.1021/acs.chemmater.6b03928
Chem. Mater. 2017, 29, 1076−1088

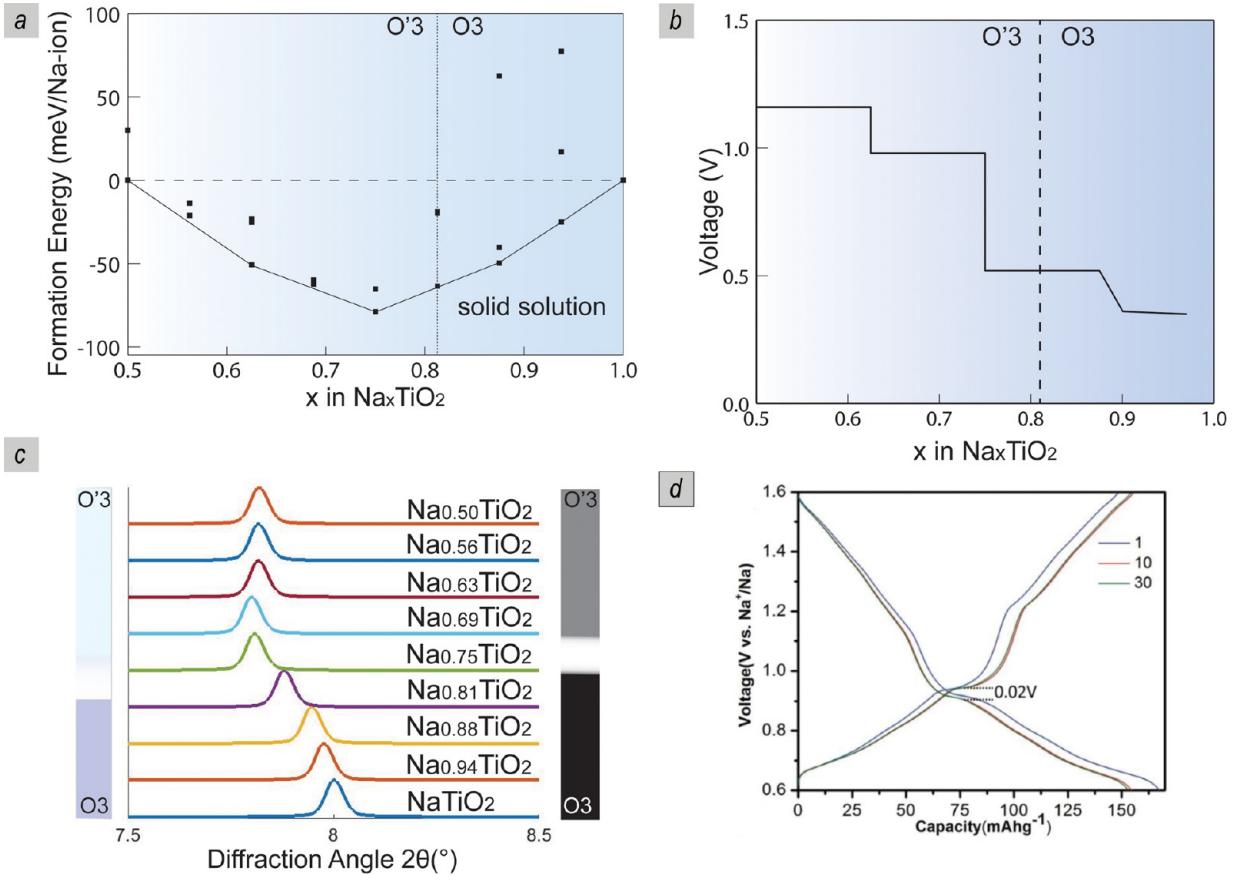

Figure 7. a: Convex hull based on DFT calculations of the layered Na_xTiO_2 structure for $0.5 < x < 1.0$. b: Voltage profile of Na intercalation in the O3/O′3 layered Na_xTiO_2. c: Calculated powder diffraction data from the lowest energy configurations at each concentration step. The left bar indicates the predicted O3 and O′3 regimes, and the bar on the right side indicates the experimentally found O3 and O′3 regimes based on in situ XRD.[25] d: Experimental voltage profile reproduced from ref 25 with permission from The Royal Society of Chemistry.

$$\bar{V}(x) = -\frac{E_{Na_xTiO_2} - xE_{Na} - E_{TiO_2}}{xe}$$

where $\bar{V}$ is the average intercalation voltage, and the energies represent total energies of the indicated compositions. The voltage profile is depicted in Figure 5b. As discussed for the formation energies in Figure 5a a solid solution reaction is expected between TiO_2 (H) and $Na_{0.25}TiO_2$ (H). However, the voltage plateaus in Figure 7 appear at 0 K because the formation energies of $Na_{0.063}TiO_2$ (H) and $Na_{0.19}TiO_2$ (H) are located only a few meV above the convex hull. Following the most stable convex hull in Figure 5a this is followed by a first-order phase transition to the layered $Na_{0.68}TiO_2$ (L) structure. However, as discussed above, in practice the hollandite structure appears to be maintained following the dashed voltage curve shown in Figure 5b.

3.4. Toward the O3 Layered $NaTiO_2$ Structure. The DFT calculations predict that sodiation of the hollandite structure up to the $NaTiO_2$ composition results in the layered O3 type $NaTiO_2$ phase, characterized by the hexagonal $R\bar{3}m$ group (note that an equivalent definition in the monoclinic phase $C2/m$ is also possible). Na-ions in the O3 lattice are octahedral coordinated oxygen atoms, while the transition metal (Ti) stacking has a repetition of three in the perpendicular direction to Na layers (c-axis).[25,75] Table 4 compares the structure of the predicted layered $NaTiO_2$ composition with that reported experimentally.[25] DFT significantly overestimated the c-lattice parameter (by 0.3 Å).

Table 4. Comparison between Experimental and Calculation Results for the O3 Layered $NaTiO_2$ Structure (Unit Cell)

method	experiment value[25]	experimental values relaxed with DFT	predicted values upon sodiating with DFT
s.g.	R-3M	R-3M	R-3M
a (Å)	3.037(1)	2.991	2.993
b (Å)	3.037(1)	2.991	2.993
c (Å)	16.260(2)	16.569	16.5713
γ (Å)	120	120	120
ΔE (meV)		0	+15

In the equivalent $C2/m$ definition this translates into a significantly smaller β° angle, 97° compared to 107.9° reported experimentally.[25]

To investigate the properties of the layered structure, the configurations in the $0.5 < x < 1$ compositional range were calculated by DFT (note that the energies of the layered $0.68 < x < 1$ compositions were already shown in Figure 5). The resulting convex hull is presented in Figure 7a, and the voltage profile is presented in Figure 7b. The convex hull depicts a solid solution intercalation mechanism throughout the sodiation range ($0.5 < x < 1$) as the lowest energy configurations are on or slightly above ($\ll$25 meV) the convex hull. The DFT calculations predict that the O3 to O′3 transition occurs at $Na_{0.81}TiO_2$ in good agreement with the experimental observation by Wu et al.[25] XRD patterns were calculated based on the most stable configurations (located on the convex

DOI: 10.1021/acs.chemmater.6b03928
Chem. Mater. 2017, 29, 1076−1088

hull in Figure 7a). The results are shown in Figure 7c focusing on small diffraction angles in order to distinguish the O3 and O′3 phases. Volume changes calculated in the layered regime are almost negligible (0.8%) prolonging excellent cycle-life, in agreement with the 0.4% volume change determined experimentally.[25] The calculated voltage profile is in agreement with the experimental one,[25] predicting slightly lower voltages, an underestimation which is common when utilizing the GGA method.[76]

3.5. Na-Ion Diffusion. To predict the Na-ion diffusion mechanism in the hollandite and layered titanate structures, molecular dynamic (MD) calculations were performed at 600 K for total simulation times ranging from 190 to 400 ps. In addition, solid state nudge elastic band methods (NEB, ss-NEB[50]) were used to predict the energy barriers for diffusion. In the hollandite structure the diffusion pathway is one-dimensional through the 2 × 2 tunnels parallel to the *z*-axis. An overview of possible jumps is presented in Figure 8.

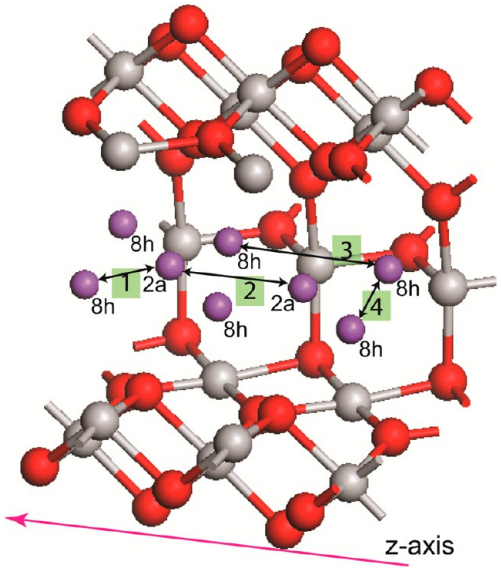

Figure 8. Possible jumps inside the 2 × 2 hollandite tunnels where the 1, 2, and 3 jumps can contribute to macroscopic diffusion, and jump number 4 represents a coplanar local jump not contributing to the macroscopic diffusion.

Within the dilute concentration range ($0 < x < 0.125$), where the structure is tetragonal, there is a single Na-ion per pair of adjacent 2 × 2 hollandite tunnels along the *z*-direction. This creates a large variety of possible hops due to the large available space offered by the 2 × 2 tunnel. Our results depict extremely high jump rates along the *z*-direction either by a direct 2a-2a jump passing through the intermediate 2b position (2a-2b-2a) or by a curved hop passing through an intermediate 8h position (2a-8h-2a). The Na-ion density obtained from the MD simulation performed in the dilute limit, shown in Figure 9a, b, demonstrates that the Na-ion is highly mobile as it appears broadly delocalized around the lowest energy 2a position. It partially occupies the less favorable 4e position (see Table 2) during the majority of the simulation time (>70%). The maximum Na-ion density is predicted to be located at the lowest energy 2a site where it is located approximately 20% of the total simulation time. Fluctuations around the 2a positions indicate that the Na-ion jumps back and forth toward the coplanar 8h′ position. Consistent with the thermodynamic analysis, the 8h′ site is energetically unfavorable (see Table 2) forcing the Na-ion back to the 2a position during the calculation on average within 6 femto seconds. Even larger oscillations occur near the 4e positions, during the transition between two adjacent 2a sites, building up momentum to initiate a subsequent transition. Figure 9a depicts a large number of these curved Na-ion pathways near the 4e position, and Figure 9c illustrates a schematic representation of the oscillations. By counting the number of hops between the respective interstitial sites during the 200 ps MD simulation the energy barriers can be predicted, see Methods section, which appear in excellent agreement with the ss-NEB results shown in Table 5. However, a significantly different 2a-8h energy barrier is found compared to NEB without lattice parameter relaxations. MD simulations take into account the lattice dynamics, which are also better captured by the ss-NEB methods,[50] indicating the importance of the lattice dynamics for the Na-ion diffusion in the hollandite structure. In addition, the 2a-8h transitions appear to activate the tetragonal to monoclinic phase transition, which is accompanied by a change in the lattice parameter, a process that is also better captured by ss-NEB calculations.[50]

The molecular dynamic simulations also reveal that a 2a-8h jump may result in occupation of the 8h site for a few picoseconds, indicating this site to be metastable. Remaining in the xy-plane the Na-ion is shown to easily jump toward the coplanar 8h position (8h-2b-8h) before it relaxes toward the lower energy 2a site. In addition, many transitions go through multiple sites where the most frequently occurring are the 2a-8h-2b-2a, 2a-2b-8h-2a, and 2a-8h′-8h-8h′-2a site sequences. This can be attributed to the low energy barrier and small jump distance for coplanar hops (8h′-2a, 2b-8h) as illustrated by Table 5.

The Na-ion kinetics in the monoclinic concentration range ($0.125 < x < 0.25$) are very similar to that in the dilute limit. Adjacent tunnels with only one Na-ion behave identical with respect the dilute limit analysis presented above. Upon the introduction of a second Na-ion per adjacent tunnels, Na migration from the 2a site to the 8h site is initiated enabling the observed phase transition (from tetragonal to monoclinic), a transition easily activated according to our calculations.

However, in the $Na_{0.25}TiO_2$ (H) phase, where the zigzag occupancy of the 8h sites appears most stable, the Na-ion diffusion changes drastically. Figure 10a, b illustrates the Na-ion density plot resulting from the MD simulation of the respective phase for 400 ps at 600 K. In contrast to the connected Na-ion density between adjacent 2 × 2 tunnels at the dilute limit, the Na-ion densities around the 8h positions appear at this composition almost isolated, indicating poor mobility along the diffusion coordinate. Within the 400 ps simulation time only a couple of forward transitions in the *z*-direction occurred during the simulation, depicted by the thin light-green paths in Figure 10a, b. Apparently, the energy barrier for diffusion is too large to be probed quantitatively by the MD simulations due to the limited simulation time. A larger number of transitions are predicted to occur between the coplanar 8h sites; however, these reflect local jumps that do not contribute to the macroscopic diffusion. The MD simulations reveal that the local coplanar 8h-8h jumps are highly correlated with the local coplanar 8h-8h jumps in the adjacent 2 × 2 tunnel. The Na-ion hops occur simultaneously for both adjacent Na-ions thereby maintaining the lowest energy zigzag configuration, most likely driven by Coulombic repulsions to maximize the distance

DOI: 10.1021/acs.chemmater.6b03928
Chem. Mater. 2017, 29, 1076−1088

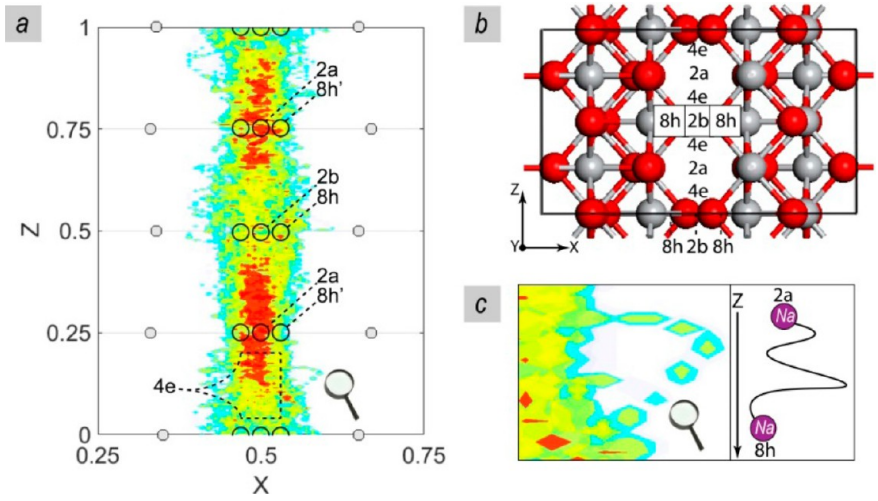

Figure 9. a Na-ion density plot in the xz-plane integrated over the 200 ps molecular dynamic calculation for the dilute limit $Na_{0.06}TiO_2$ (only one Na-ion in the supercell). From red to blue represents the decreasing Na-ion density. The gray dots represent the nearest Ti atoms (left and right) of the tunnel. The various interstitial sites are indicated. In order to make the 2a and 2b positions in the xz-plane visible the 8h′ and 8h positions that are perpendicular to the *z*-axis (and consequently hiding the 2a and 2b positions) are not indicated. b: The xz-plane in the supercell for comparison with part a. c: Zoom in to one of the Na-ion paths caused by oscillations near the 4e position and schematic representation of the oscillating mechanism that dominates the 2a-8h hop.

Table 5. Energy Barriers for Na Diffusion Calculated by NEB, ss-NEB, and the MD Simulations[a]

x in Na_xTiO2	Path illustration	Path	Method	E_a (Na-ion) (eV)	Distance(Å)
x=0.03 (H)	2	2a–(2b)-2a	NEB	0.32	2.98
x=0.03 (H)	2	2a-(2b)-2a	SS-NEB	**0.16**	2.98
x=0.06 (H)	2	2a-(2b)-2a	MD	**0.15**	2.98
x=0.03 (H)	1	2a-8h	NEB	0.72	1.68
x=0.03 (H)	1	2a-8h	SS-NEB	**0.12**	1.68
x=0.06 (H)	1	2a-8h	MD	**0.19**	1.68
x=0.06 (H)	4	8h-8h (in plane)	MD	0.26	1.325/1.874
x=0.06 (H)	-	2b-8h (in plane)	MD	0.19	0.937
x=0.06 (H)	-	8h-2b (in plane)	MD	0.19	0.937
x=0.25 (H)	coupled	8h-8h (in plane)	MD	0.15	1.325/1.874
x=0.25 (H)	-	8h-2b (in plane)	MD	0.23	0.937
x=0.25 (H)	coupled	8h-8h forward	MD	∞	2.97
x=0.31 (H)	3	8h-8h forward	NEB	0.68	2.97
x=0.31 (H)	coupled	8h-8h forward	MD	∞	2.97
x=0.75 (L)	-	divacancy	MD	0.28	3.10

[a]Numbers in path illustration indicate the paths presented in Figure 8.

between the Na-ions. This mechanism is depicted in Figure 10d, e. Another correlated reaction mechanism, qualitatively captured by the MD simulations, governs the forward jump depicted in Figure 10c. This correlated jump is initiated in the middle of a 8h-8h coplanar hop where additional Na-ion fluctuations lead to Coulombic interactions that result in Na-ion migration along the *z*-direction and thus macroscopic diffusion. In addition, a 200 ps molecular dynamic simulation for the $Na_{0.31}TiO_2$ (H) phase was performed where a third Na-ion is introduced per pair of adjacent 2 × 2 tunnels. The MD simulations result in no macroscopic and coplanar diffusion as the interactions between Na-ions dominate, resulting in even more localized Na-ion densities (not shown) compared to that in Figure 10. In this configuration the 8h-8h forward jump presented in Figure 8 appears to contribute to macroscopic diffusion. At this concentration the NEB calculations did not converge, most likely due to the close coexistence of Na-ions in the tunnel. Analysis beyond the dilute limit has been shown before to be less trivial as the significant Na concentration causes interactions between the charged carriers.[77] Nevertheless, the 8h-8h forward jump was calculated after removing all but one hopping Na-ion in the lattice parameters of the $Na_{0.31}TiO_2$ phase revealing an extremely high barrier of 0.68 eV, in qualitative agreement with the present MD results that indicate poor Na-ion dynamics.

DOI: 10.1021/acs.chemmater.6b03928
Chem. Mater. 2017, 29, 1076−1088

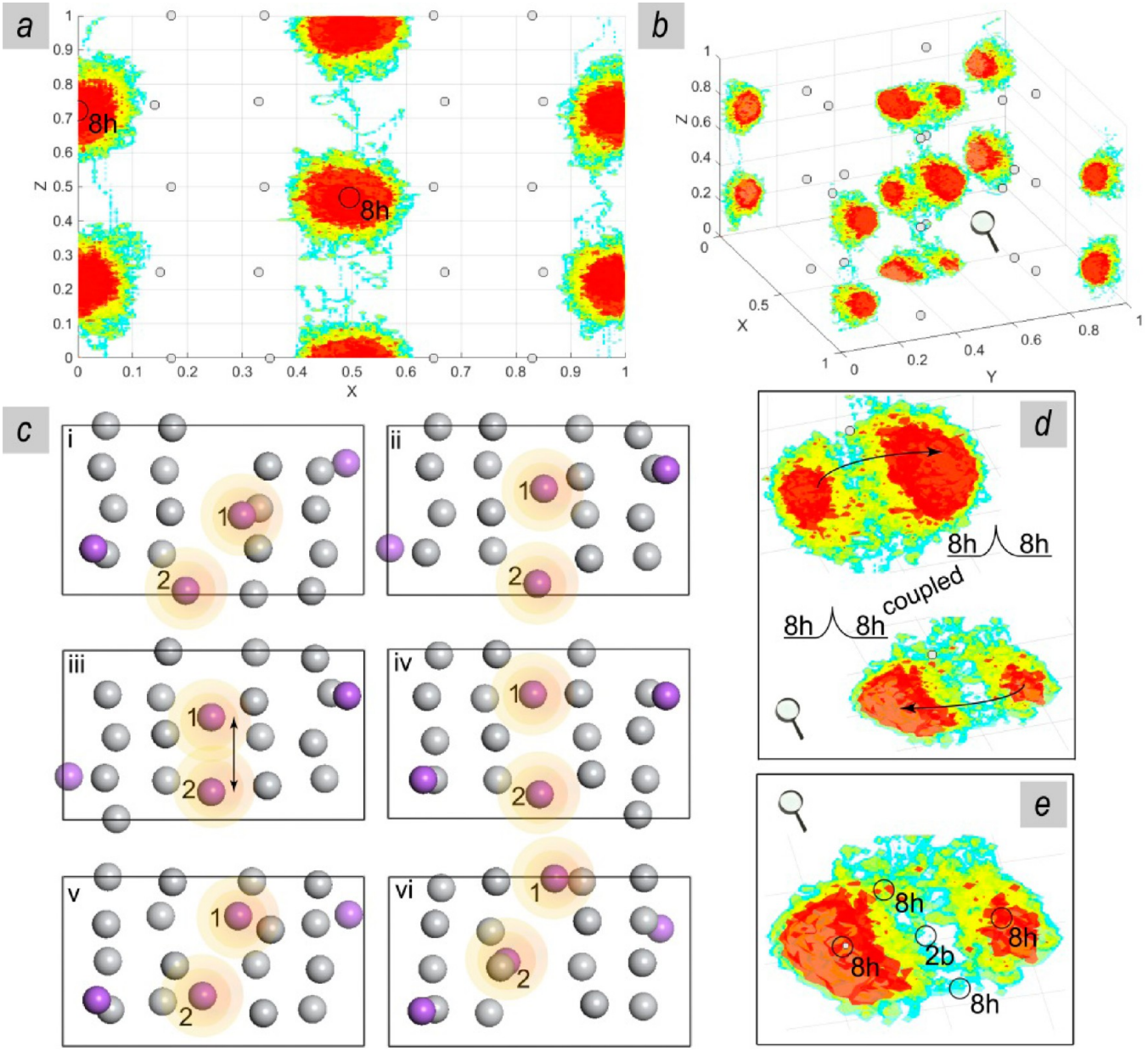

Figure 10. a, b: 3D Na-ion density plot integrated over the 400 ps of molecular dynamic calculation of $Na_{0.25}TiO_2$ (4 Na-ions in the supercell). c: Time lapse in the xz-plane illustrating a simultaneous forward jump. d: Transition mechanism showing the correlated Na-ion 8h-8h coplanar hops thereby maintaining the preferable Na-ion zigzag configuration, presented in the same plane as part b. e: Zoom of the Na-ion density to indicate the relevant interstitial positions, the 2b and 8h positions exist in the xy-plane that is perpendicular to the *z*-axis where macroscopic diffusion occurs.

The Na-ion kinetics in the layered O3/O′3 Na_xTiO_2 has already been studied in detail by Wu et al.[25] who applied the nudge elastic band method, utilizing the divacancy hopping mechanism.[78] The resulted barriers were reported to be smaller than 0.22 eV, for both the O3 and O3 layered configurations indicating exceptionally good kinetics.[25] This result is in contrast to previous reports indicating a large barrier of 0.75 eV.[30] For comparison, we performed a 190 ps MD simulation of the O′3 $Na_{0.75}TiO_2$ phase at 600 K. The calculated activation energy (see methods) for Na-ion migration was found to be 0.28 eV in good agreement with the results reported by Wu et al.[25] The divacancy hopping mechanism, that is considered dominant regarding Na and Li-ion hopping in O3 layers,[25,78,79] dictates that the Na-ion diffusion occurs through an adjacent tetrahedral site that acts as a local minimum. This mechanism was clearly observed during the MD simulation as shown in Figure 11.

Based on the activation energy calculations, an estimate of the diffusion coefficient was calculated using the random-walk atomistic model and, when applicable, the mean square displacement (MSD) obtained from the molecular dynamic calculations (see the Methods section). The diffusion coefficient at room temperature ranges from $D_{TST} = 9.65 \cdot 10^{-6}$ to $4.2 \cdot 10^{-9}$ cm^2/s at the dilute limit decreasing to $D_{TST} = 3.8 \cdot 10^{-15}$ cm^2/s at higher Na concentrations ($x = 0.31$), indicating that Na-ion insertion beyond $Na_{0.25}TiO_2$ (H) is difficult. In addition, the presence of defects in the 1D diffusion tunnels can be expected to lower these diffusion coefficients, motivating nanostructuring to enable usage of the thermodynamically feasible $Na_{0.5}TiO_2$ phase. For the layered structure we

DOI: 10.1021/acs.chemmater.6b03928
Chem. Mater. 2017, 29, 1076−1088

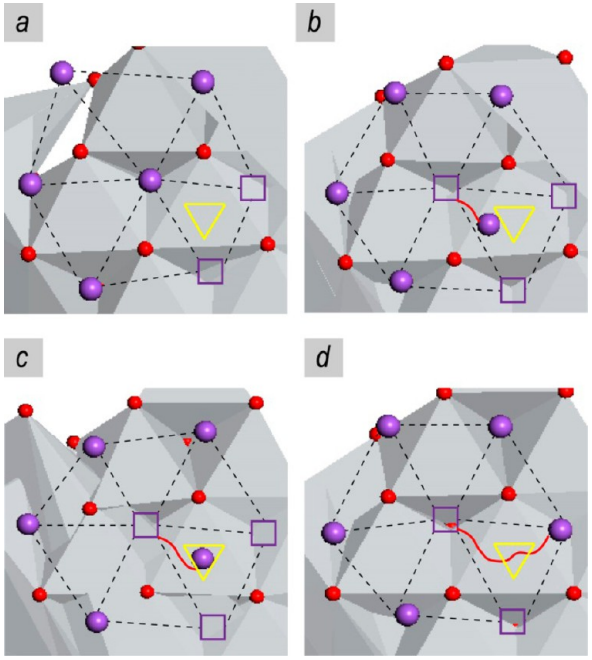

Figure 11. Divacancy hopping mechanism as seen perpendicularly to the plane formed by Na-ions, the Na-ion passes through a tetrahedral site illustrated by the yellow triangle. The sequence is completed within 1.2 ps.

obtained $D_{MSD} = 5.7 \cdot 10^{-9}$ cm^2/s, based on the MSD at room temperature and $D_{TST} = 6.3 \cdot 10^{-8}$ cm^2/s based on transitional state theory. The second value is significantly larger because it takes into account back and forth jumps that do not contribute in macroscopic diffusion. This large diffusion coefficient is in good agreement with rate capability experiments[25] underlining that the layered structure is a promising anode for Na-ion batteries.

4. CONCLUDING REMARKS

The present DFT study of the thermodynamic and kinetic properties of Na-ion insertion in hollandite TiO_2 brings forward a detailed understanding of the phase transition behavior and Na-ion kinetics showing good agreement with most of the experimental observations. Initially, Na-ion insertion leads to a solid solution reaction causing a monoclinic symmetry reduction ($I4/m$ to $I2/m$) toward the $Na_{0.25}TiO_2$ composition. During this transformation the structural changes are very small suggesting a promising cycle life. In the dilute limit, low energy barriers are predicted suggesting fast Na-ion diffusion at the early stages of insertion. At the $Na_{0.25}TiO_2$ composition and beyond, the Na-ion diffusion drops dramatically, giving a rational for the experimental observation that Na-ion insertion does not proceed beyond $Na_{0.25}TiO_2$ phase, although the DFT predicts that the $Na_{0.5}TiO_2$ composition can be achieved at 0.4 V vs Na/Na$^+$.

Detailed consideration of the Na-ion kinetics from the molecular dynamic (MD) simulations shows that large space of the 2 × 2 tunnel in the hollandite structure results in complex atomic transitions that appear responsible for the high Na-ion mobility at the early stages of Na-ion insertion. MD simulations beyond the dilute limit reveal a highly correlated diffusion mechanism within the 2 × 2 tunnel, most likely driven by the strong Coulombic interactions between the Na-ions that lowers the number of successful transitions. These results are anticipated to be of general importance to similar structured materials such as MnO_2 hollandite.

At larger Na-ion concentrations, a first-order phase transformation is predicted toward the O′3-$Na_{0.63}$TiO2 endmember structure. Further Na-ion insertion initiates a solid solution reaction that results in the layered O3-$NaTiO_2$ material, a promising anode candidate with a large capacity reported previously. The full thermodynamic path (TiO_2 (H) to O3-$NaTiO_2$), however, is not reversible but may be considered an alternative preparation route toward the layered structure. So far the layered O3-$NaTiO_2$ material is being prepared via a solid state reaction to reduce anatase - TiO_2[25,73,80] requiring high temperatures up to 1000 °C in the presence of Na-metal under an argon flow for several hours. Although the preparation of hollandite is also not facile, as it requires mixing of K_2CO_3 and anatase TiO_2 for 8 h followed by acid treatment to remove K at low temperatures for 10 h,[37] using TiO_2 (H) as a starting material might present an opportunity for a preparation route toward the layered material requiring lower annealing temperatures.

Within the layered Na_xTiO_2 regime a solid solution insertion mechanism transforms the O3 layered Na_xTiO_2 structure for compositions $1 < x < 0.81$ to the O′3 layered Na_xTiO_2 structure for compositions $0.81 < x < 0.5$, in good agreement with experiments. For the O′3 $Na_{0.75}TiO_2$ phase the MD simulations capture the predicted divacancy hopping mechanism, calculating a small energy barrier (0.27 eV) that suggests excellent Na-ion kinetics.

AUTHOR INFORMATION

Corresponding Author

*E-mail: m.wagemaker@tudelft.nl.

ORCID

Marnix Wagemaker: 0000-0003-3851-1044

Notes

The authors declare no competing financial interest.

ACKNOWLEDGMENTS

The research leading to these results has received funding from the European Research Council under the European Union's Seventh Framework Program (FP/2007-2013)/ERC Grant Agreement n. [307161] of MW. We thank Jouke Heringa for technical support.

REFERENCES

(1) Kundu, D.; Talaie, E.; Duffort, V.; Nazar, L. F. The Emerging Chemistry of Sodium Ion Batteries for Electrochemical Energy Storage. *Angew. Chem., Int. Ed.* **2015**, *54*, 3431−3448.

(2) Kim, S. W.; Seo, D. H.; Ma, X. H.; Ceder, G.; Kang, K. Electrode Materials for Rechargeable Sodium-Ion Batteries: Potential Alternatives to Current Lithium-Ion Batteries. *Adv. Energy Mater.* **2012**, *2*, 710−721.

(3) Palomares, V.; Casas-Cabanas, M.; Castillo-Martinez, E.; Han, M. H.; Rojo, T. Update on Na-based battery materials. A growing research path. *Energy Environ. Sci.* **2013**, *6*, 2312−2337.

(4) Kubota, K.; Komaba, S. Review-Practical Issues and Future Perspective for Na-Ion Batteries. *J. Electrochem. Soc.* **2015**, *162*, A2538−A2550.

(5) Sawicki, M.; Shaw, L. L. Advances and challenges of sodium ion batteries as post lithium ion batteries. *RSC Adv.* **2015**, *5*, 53129−53154.

(6) Asher, R. C. A Lamellar Compound of Sodium and Graphite. *J. Inorg. Nucl. Chem.* **1959**, *10*, 238.

DOI: 10.1021/acs.chemmater.6b03928
Chem. Mater. 2017, 29, 1076−1088

(7) Stevens, D. A.; Dahn, J. R. The mechanisms of lithium and sodium insertion in carbon materials. *J. Electrochem. Soc.* **2001**, *148*, A803−A811.
(8) Luo, W.; Bommier, C.; Jian, Z. L.; Li, X.; Carter, R.; Vail, S.; Lu, Y. H.; Lee, J. J.; Ji, X. L. Low-Surface-Area Hard Carbon Anode for Na-Ion Batteries via Graphene Oxide as a Dehydration Agent. *ACS Appl. Mater. Interfaces* **2015**, *7*, 2626−2631.
(9) Alcantara, R.; Mateos, J. M. J.; Tirado, J. L. Negative electrodes for lithium and sodium-ion batteries obtained by heat-treatment of petroleum cokes below 1000 degrees C. *J. Electrochem. Soc.* **2002**, *149*, A201−A205.
(10) Jow, T. R.; Shacklette, L. W.; Maxfield, M.; Vernick, D. The Role of Conductive Polymers in Alkali-Metal Secondary Electrodes. *J. Electrochem. Soc.* **1987**, *134*, 1730−1733.
(11) Didier, C.; Guignard, M.; Denage, C.; Szajwaj, O.; Ito, S.; Saadoune, I.; Darriet, J.; Delmas, C. Electrochemical Na-Deintercalation from $NaVO_2$. *Electrochem. Solid-State Lett.* **2011**, *14*, A75−A78.
(12) Kim, H.; Kim, D. Y.; Kim, Y.; Lee, S. S.; Park, K. Na Insertion Mechanisms in Vanadium Oxide Nanotubes for Na-Ion Batteries. *ACS Appl. Mater. Interfaces* **2015**, *7*, 1477−1485.
(13) Deng, J. Q.; Lu, Z. G.; Belharouak, I.; Amine, K.; Chung, C. Y. Preparation and electrochemical properties of $Li_4Ti_5O_{12}$ thin film electrodes by pulsed laser deposition. *J. Power Sources* **2009**, *193*, 816−821.
(14) Kavan, L.; Prochazka, J.; Spitler, T. M.; Kalbac, M.; Zukalova, M. T.; Drezen, T.; Gratzel, M. Li insertion into $Li_4Ti_5O_{12}$ (Spinel) - Charge capability vs. particle size in thin-film electrodes. *J. Electrochem. Soc.* **2003**, *150*, A1000−A1007.
(15) Ohzuku, T.; Ueda, A.; Yamamoto, N. Zero-Strain Insertion Material of $Li[Li_{1/3}Ti_{5/3}]O_4$ for Rechargeable Lithium Cells. *J. Electrochem. Soc.* **1995**, *142*, 1431−1435.
(16) Colbow, K. M.; Dahn, J. R.; Haering, R. R. Structure and Electrochemistry of the Spinel Oxides $LiTi_2O_4$ and $Li_{4/3}Ti_{5/3}O_4$. *J. Power Sources* **1989**, *26*, 397−402.
(17) Wagemaker, M.; Borghols, W. J. H.; van Eck, E. R. H.; Kentgens, A. P. M.; Kearley, G. L.; Mulder, F. M. The influence of size on phase morphology and Li-ion mobility in nanosized lithiated anatase TiO_2. *Chem. - Eur. J.* **2007**, *13*, 2023−2028.
(18) Koudriachova, M. V.; Harrison, N. M.; de Leeuw, S. W. Open circuit voltage profile for Li-intercalation in rutile and anatase from first principles. *Solid State Ionics* **2002**, *152-153*, 189−194.
(19) Cava, R. J.; Murphy, D. W.; Zahurak, S.; Santoro, A.; Roth, R. S. The Crystal-Structures of the Lithium-Inserted Metal-Oxides $Li_{0.5}TiO_2$ Anatase, $LiTi_2O_4$ Spinel, and $Li_2Ti_2O_4$. *J. Solid State Chem.* **1984**, *53*, 64−75.
(20) Rai, A. K.; Anh, L. T.; Gim, J.; Mathew, V.; Kang, J.; Paul, B. J.; Song, J.; Kim, J. Simple synthesis and particle size effects of TiO_2 nanoparticle anodes for rechargeable lithium ion batteries. *Electrochim. Acta* **2013**, *90*, 112−118.
(21) Pfanzelt, M.; Kubiak, P.; Fleischhammer, M.; Wohlfahrt-Mehrens, M. TiO2 rutile-An alternative anode material for safe lithium-ion batteries. *J. Power Sources* **2011**, *196*, 6815−6821.
(22) Chiba, K.; Kijima, N.; Takahashi, Y.; Idemoto, Y.; Akimoto, J. Synthesis, structure, and electrochemical Li-ion intercalation properties of $Li_2Ti_3O_7$ with $Na_2Ti_3O_7$-type layered structure. *Solid State Ionics* **2008**, *178*, 1725−1730.
(23) Aravindan, V.; Lee, Y. S.; Yazami, R.; Madhavi, S. TiO_2 polymorphs in 'rocking-chair' Li-ion batteries. *Mater. Today* **2015**, *18*, 345−351.
(24) Wu, L. M.; Bresser, D.; Buchholz, D.; Giffin, G. A.; Castro, C. R.; Ochel, A.; Passerini, S. Unfolding the Mechanism of Sodium Insertion in Anatase TiO_2 Nanoparticles. *Adv. Energy Mater.* **2015**, *5*, 1401142.
(25) Wu, D.; Li, X.; Xu, B.; Twu, N.; Liu, L.; Ceder, G. NaTiO2: a layered anode material for sodium-ion batteries. *Energy Environ. Sci.* **2015**, *8*, 195−202.
(26) Wu, L. M.; Buchholz, D.; Bresser, D.; Chagas, L. G.; Passerini, S. Anatase TiO_2 nanoparticles for high power sodium-ion anodes. *J. Power Sources* **2014**, *251*, 379−385.
(27) Zhao, L.; Pan, H. L.; Hu, Y. S.; Li, H.; Chen, L. Q. Spinel lithium titanate ($Li_4Ti_5O_{12}$) as novel anode material for room-temperature sodium-ion battery. *Chin. Phys. B* **2012**, *21*, 028201.
(28) Sun, Y.; Zhao, L.; Pan, H. L.; Lu, X.; Gu, L.; Hu, Y. S.; Li, H.; Armand, M.; Ikuhara, Y.; Chen, L. Q.; Huang, X. J. Direct atomic-scale confirmation of three-phase storage mechanism in $Li_4Ti_5O_{12}$ anodes for room-temperature sodium-ion batteries. *Nat. Commun.* **2013**, *4*, 1870.
(29) Delmas, C.; Maazaz, A.; Hagenmuller, P. Crystal-Chemistry and Fast Ionic-Conductivity of Sodium and Potassium Phases Having Cristobalite-Related Structures. *Solid State Ionics* **1983**, *9−10*, 83−88.
(30) Wang, Y. S.; Yu, X. Q.; Xu, S. Y.; Bai, J. M.; Xiao, R. J.; Hu, Y. S.; Li, H.; Yang, X. Q.; Chen, L. Q.; Huang, X. J. A zero-strain layered metal oxide as the negative electrode for long-life sodium-ion batteries. *Nat. Commun.* **2013**, *4*, 2365.
(31) Lei, Y. C.; Li, X.; Liu, L.; Ceder, G. Synthesis and Stoichiometry of Different Layered Sodium Cobalt Oxides. *Chem. Mater.* **2014**, *26*, 5288−5296.
(32) Latroche, M.; Brohan, L.; Marchand, R.; Tournoux, M. New Hollandite Oxides - TiO_2(H) and $K_{0.06}TiO_2$. *J. Solid State Chem.* **1989**, *81*, 78−82.
(33) Noailles, L. D.; Johnson, C. S.; Vaughey, J. T.; Thackeray, M. M. Lithium insertion into hollandite-type TiO_2. *J. Power Sources* **1999**, *81-82*, 259−263.
(34) Gutierrez-Florez, M. T.; Kuhn, A.; Garcia-Alvarado, F. Lithium intercalation in $K_xTi_8O_{16}$ compounds. *Int. J. Inorg. Mater.* **1999**, *1*, 117−121.
(35) Sakao, M.; Kijima, N.; Akimoto, J.; Okutani, T. Synthesis, crystal structure, and electrochemical properties of hollandite-type $K_{0.008}TiO_2$. *Solid State Ionics* **2012**, *225*, 502−505.
(36) Sakao, M.; Kijima, N.; Akimoto, J.; Okutani, T. Lithium insertion and extraction properties of hollandite-type K_xTiO_2 with different K content in the tunnel space. *Solid State Ionics* **2013**, *243*, 22−29.
(37) Perez-Flores, J. C.; Baehtz, C.; Kuhn, A.; Garcia-Alvarado, F. Hollandite-type TiO_2: a new negative electrode material for sodium-ion batteries. *J. Mater. Chem. A* **2014**, *2*, 1825−1833.
(38) Kresse, G.; Furthmuller, J. Efficiency of ab-initio total energy calculations for metals and semiconductors using a plane-wave basis set. *Comput. Mater. Sci.* **1996**, *6*, 15−50.
(39) Blochl, P. E. Projector Augmented-Wave Method. *Phys. Rev. B: Condens. Matter Mater. Phys.* **1994**, *50*, 17953−17979.
(40) Perdew, J. P.; Burke, K.; Ernzerhof, M. Generalized gradient approximation made simple. *Phys. Rev. Lett.* **1996**, *77*, 3865−3868.
(41) Anisimov, V. I.; Zaanen, J.; Andersen, O. K. Band Theory and Mott Insulators - Hubbard-U Instead of Stoner-I. *Phys. Rev. B: Condens. Matter Mater. Phys.* **1991**, *44*, 943−954.
(42) Anisimov, V. I.; Solovyev, I. V.; Korotin, M. A.; Czyzyk, M. T.; Sawatzky, G. A. Density-Functional Theory and Nio Photoemission Spectra. *Phys. Rev. B: Condens. Matter Mater. Phys.* **1993**, *48*, 16929−16934.
(43) Morgan, B. J.; Watson, G. W. Role of Lithium Ordering in the Li_xTiO_2 Anatase -> Titanate Phase Transition. *J. Phys. Chem. Lett.* **2011**, *2*, 1657−1661.
(44) Zhou, F.; Cococcioni, M.; Marianetti, C. A.; Morgan, D.; Ceder, G. First-principles prediction of redox potentials in transition-metal compounds with LDA + U. *Phys. Rev. B: Condens. Matter Mater. Phys.* **2004**, *70*, 235121.
(45) Fabris, S.; de Gironcoli, S.; Baroni, S.; Vicario, G.; Balducci, G. Taming multiple valency with density functionals: A case study of defective ceria. *Phys. Rev. B: Condens. Matter Mater. Phys.* **2005**, *71*, 041102.
(46) Hu, Z. P.; Metiu, H. Choice of U for DFT plus U Calculations for Titanium Oxides. *J. Phys. Chem. C* **2011**, *115*, 5841−5845.
(47) Henkelman, G.; Jonsson, H. Improved tangent estimate in the nudged elastic band method for finding minimum energy paths and saddle points. *J. Chem. Phys.* **2000**, *113*, 9978−9985.

DOI: 10.1021/acs.chemmater.6b03928
Chem. Mater. 2017, 29, 1076−1088

(48) Henkelman, G.; Uberuaga, B. P.; Jonsson, H. A climbing image nudged elastic band method for finding saddle points and minimum energy paths. *J. Chem. Phys.* **2000**, *113*, 9901−9904.
(49) Sheppard, D.; Terrell, R.; Henkelman, G. Optimization methods for finding minimum energy paths. *J. Chem. Phys.* **2008**, *128*, 134106.
(50) Sheppard, D.; Xiao, P. H.; Chemelewski, W.; Johnson, D. D.; Henkelman, G. A generalized solid-state nudged elastic band method. *J. Chem. Phys.* **2012**, *136*, 074103.
(51) Morgan, D.; Van der Ven, A.; Ceder, G. Li conductivity in Li_xMPO_4 (M = Mn, Fe, Co, Ni) olivine materials. *Electrochem. Solid-State Lett.* **2004**, *7*, A30−A32.
(52) Vineyard, G. H. Frequency Factors and Isotope Effects in Solid State Rate Processes. *J. Phys. Chem. Solids* **1957**, *3*, 121−127.
(53) Van der Ven, A.; Ceder, G.; Asta, M.; Tepesch, P. D. First-principles theory of ionic diffusion with nondilute carriers. *Phys. Rev. B: Condens. Matter Mater. Phys.* **2001**, *64*, 18430.
(54) Yamada, A.; Chung, S. C.; Hinokuma, K. Optimized $LiFePO_4$ for lithium battery cathodes. *J. Electrochem. Soc.* **2001**, *148*, A224−A229.
(55) Kutner, R. Chemical Diffusion in the Lattice Gas of Non-Interacting Particles. *Phys. Lett. A* **1981**, *81*, 239−240.
(56) de Klerk, N. J. J.; Wagemaker, M. Diffusion Mechanism of the Sodium-Ion Solid Electrolyte Na_3PS_4 and Potential Improvements of Halogen Doping. *Chem. Mater.* **2016**, *28*, 3122−3130.
(57) Lee, S. H.; Kang, J. H.; Kang, M. H. Structural properties of semiconductors in the generalized gradient approximation. *J. Korean Phys. Soc.* **1997**, *31*, 811−814.
(58) Tompsett, D. A.; Islam, M. S. Electrochemistry of Hollandite alpha-MnO_2: Li-Ion and Na-Ion Insertion and Li_2O Incorporation. *Chem. Mater.* **2013**, *25*, 2515−2526.
(59) Kingery, W. D.; Chiang, Y.-M.; Birnie, D. *Physical Ceramics: Principles for Ceramic Science and Engineering*; Wiley: USA, 1997.
(60) Wagemaker, M.; Kearley, G. J.; van Well, A. A.; Mutka, H.; Mulder, F. M. Multiple li positions inside oxygen octahedra in lithiated TiO_2 anatase. *J. Am. Chem. Soc.* **2003**, *125*, 840−848.
(61) Koudriachova, M. V.; Harrison, N. M.; de Leeuw, S. W. Density-functional simulations of lithium intercalation in rutile. *Phys. Rev. B: Condens. Matter Mater. Phys.* **2002**, *65*, 235423.
(62) Reddy, M. A.; Kishore, M. S.; Pralong, V.; Varadaraju, U. V.; Raveau, B. Lithium intercalation into nanocrystalline brookite TiO_2. *Electrochem. Solid-State Lett.* **2007**, *10*, A29−A31.
(63) Hu, Y. S.; Kienle, L.; Guo, Y. G.; Maier, J. High lithium electroactivity of nanometer-sized rutile TiO_2. *Adv. Mater.* **2006**, *18*, 1421−1426.
(64) Koudriachova, M. V.; Harrison, N. M. Li sites and phase stability in TiO2-anatase and Zr-doped TiO_2-anatase. *J. Mater. Chem.* **2006**, *16*, 1973−1977.
(65) Koudriachova, M. V.; Harrison, N. M.; de Leeuw, S. W. Effect of diffusion on lithium intercalation in titanium dioxide. *Phys. Rev. Lett.* **2001**, *86*, 1275−1278.
(66) Schmidt, W.; Bottke, P.; Sternad, M.; Gollob, P.; Hennige, V.; Wilkening, M. Small Change-Great Effect: Steep Increase of Li Ion Dynamics in $Li_4Ti_5O_{12}$ at the Early Stages of Chemical Li Insertion. *Chem. Mater.* **2015**, *27*, 1740−1750.
(67) Wagemaker, M.; Simon, D. R.; Kelder, E. M.; Schoonman, J.; Ringpfeil, C.; Haake, U.; Lutzenkirchen-Hecht, D.; Frahm, R.; Mulder, F. M. A kinetic two-phase and equilibrium solid solution in spinel $Li_{4+x}Ti_5O_{12}$. *Adv. Mater.* **2006**, *18*, 3169−3173.
(68) Santana, J. A.; Kim, J.; Kent, P. R. C.; Reboredo, F. A. Successes and failures of Hubbard-corrected density functional theory: The case of Mg doped $LiCoO_2$. *J. Chem. Phys.* **2014**, *141*, 164706.
(69) Yuan, L. X.; Wang, Z. H.; Zhang, W. X.; Hu, X. L.; Chen, J. T.; Huang, Y. H.; Goodenough, J. B. Development and challenges of $LiFePO_4$ cathode material for lithium-ion batteries. *Energy Environ. Sci.* **2011**, *4*, 269−284.
(70) Wagemaker, M.; Van Der Ven, A.; Morgan, D.; Ceder, G.; Mulder, F. M.; Kearley, G. J. Thermodynamics of spinel Li_xTiO_2 from first principles. *Chem. Phys.* **2005**, *317*, 130−136.
(71) Dalton, A. S.; Belak, A. A.; Van der Ven, A. Thermodynamics of Lithium in TiO_2(B) from First Principles. *Chem. Mater.* **2012**, *24*, 1568−1574.
(72) Van der Ven, A.; Aydinol, M. K.; Ceder, G.; Kresse, G.; Hafner, J. First-principles investigation of phase stability in Li_xCoO_2. *Phys. Rev. B: Condens. Matter Mater. Phys.* **1998**, *58*, 2975−2987.
(73) Maazaz, A.; Delmas, C.; Hagenmuller, P. A study of the Na_xTiO_2 System by electrochemical deintercalation. *J. Inclusion Phenom.* **1983**, *1*, 45−51.
(74) Aydinol, M. K.; Kohan, A. F.; Ceder, G.; Cho, K.; Joannopoulos, J. Ab initio study of lithium intercalation in metal oxides and metal dichalcogenides. *Phys. Rev. B: Condens. Matter Mater. Phys.* **1997**, *56*, 1354−1365.
(75) Delmas, C.; Fouassier, C.; Hagenmuller, P. Structural Classification and Properties of the Layered Oxides. *Physica B+C* **1980**, *99*, 81−85.
(76) Seo, D. H.; Urban, A.; Ceder, G. Calibrating transition-metal energy levels and oxygen bands in first-principles calculations: Accurate prediction of redox potentials and charge transfer in lithium transition-metal oxides. *Phys. Rev. B: Condens. Matter Mater. Phys.* **2015**, *92*, 115118.
(77) Meng, Y. S.; Arroyo-de Dompablo, M. E. First principles computational materials design for energy storage materials in lithium ion batteries. *Energy Environ. Sci.* **2009**, *2*, 589−609.
(78) Van der Ven, A.; Bhattacharya, J.; Belak, A. A. Understanding Li Diffusion in Li-Intercalation Compounds. *Acc. Chem. Res.* **2013**, *46*, 1216−1225.
(79) Van der Ven, A.; Ceder, G. Lithium diffusion in layered Li_xCoO_2. *Electrochem. Solid-State Lett.* **2000**, *3*, 301−304.
(80) Clarke, S. J.; Fowkes, A. J.; Harrison, A.; Ibberson, R. M.; Rosseinsky, M. J. Synthesis, structure, and magnetic properties of $NaTiO_2$. *Chem. Mater.* **1998**, *10*, 372−384.

DOI: 10.1021/acs.chemmater.6b03928
Chem. Mater. 2017, 29, 1076−1088